Research Article

Machine-learning-enabled composition-process co-design of heat-resistant cast aluminum alloys with superior elevated-temperature strength

Changmei Hao[1,2] Peng Kuai[1,2] Jianhua Duan[1,2] Shaolei Yang[1,2] Yudong Sui[1,2,*] Yehua Jiang[1,2,*] Han Xiao[1,2]

[1]Faculty of Materials Science and Engineering, Kunming University of Science and Technology, Kunming 650093, Yunnan, China.
[2]National & Local Joint Engineering Laboratory of Advanced Metal Solidification Forming and Equipment Technology, Kunming University of Science and Technology, Kunming 650093, Yunnan, China.

[*]**Correspondence to:** Prof. Yudong Sui, Prof. Yehua Jiang, Faculty of Materials Science and Engineering, Kunming University of Science and Technology, Kunming 650093, Yunnan, China. E-mail: suiyd2016@kust.edu.cn; jiangyehua@kmust.edu.cn

How to cite this article: Hao, C.; Kui, P.; Duan, J.; Yang, S.; Sui, Y.; Jiang, Y.; Xiao, H. Machine-learning-enabled composition-process co-design of heat-resistant cast aluminum alloys with superior elevated-temperature strength. *J Mater Inf*, 2026, *6*, [Accept]. http://dx.doi.org/10.20517/jmi.2026.20

Received: 14 April 2026 | **Revised:** 6 July 2026 | **Accepted:** 23 July 2026.

Abstract

To address the reliance on trial-and-error methods and the prolonged development cycles inherent in the composition and process design of novel cast aluminum alloys, this study constructed a multi-source feature system integrating alloy composition, physicochemical properties of elements, testing conditions, and process parameters. Employing a three-step feature selection method, a prediction model for high-temperature ultimate tensile strength (UTS) was established with a test set R^2 of 0.881 and an MAE of 22.639 MPa. Based on this model, a synergistic design of the alloy composition and heat treatment process was conducted by coupling the model with a

genetic algorithm (GA), and four novel cast aluminum alloys were experimentally validated. The experimental results indicate that the designed alloys exhibit enhanced elevated-temperature strength compared with the commercial reference alloys. Notably, the ZL-2 alloy demonstrated optimal performance, achieving a UTS of 214.2 MPa when tested at 300 °C after holding at 300 °C for 1 h. Furthermore, SHAP (SHapley Additive exPlanations) analysis revealed significant nonlinear interactions among alloy composition, testing conditions, and process parameters in determining tensile strength. Multiscale microstructural characterization reveals that the exceptional elevated-temperature strength of ZL-2 stems from the synergistic effects of nanoscale $Al_{20}Cu_2Mn_3$ and Al_2CuMg precipitates, and micron-scale Al_3Ti-containing intermetallics. This study demonstrates the application potential of data-driven methods in the composition-process synergistic design of heat-resistant cast aluminum alloys.

Keywords: Heat-resistant cast aluminum alloys, machine learning, composition-process co-design, precipitation strengthening

INTRODUCTION

Aluminum alloys, owing to their low density, high specific strength, excellent castability, and good corrosion resistance, have been widely applied in lightweight manufacturing within the automotive industry, particularly in critical powertrain components such as pistons and cylinder heads[1,2]. With the rapid development of high-power-density internal combustion engines and hybrid power systems, the service conditions faced by these hot-end components have become increasingly severe. Their operating temperatures under complex thermo-mechanical coupled loads can continuously approach 300 °C[1,3,4]. Under these conditions, the metastable strengthening phases in traditional precipitation-strengthened aluminum alloys are prone to coarsening, dissolution, or transformation into equilibrium phases, leading to a significant attenuation of the precipitation strengthening effect and ultimately triggering a rapid degradation in high-temperature mechanical properties[5]. Therefore, the development of heat-resistant cast aluminum alloys capable of maintaining high tensile strength near 300 °C has become a key scientific and engineering issue for enhancing the service reliability of engine hot-end components[6].

Focusing on the enhancement of high-temperature properties of aluminum alloys,

researchers have conducted extensive work in alloy composition design and heat treatment process optimization[7-12]. On the one hand, minor additions of Zr, Er, and Sc can promote the formation of thermally stable $L1_2$-ordered trialuminide nano-precipitates, such as Al_3Sc-, Al_3Er-, and $Al_3(Sc,Zr,Er)$-based dispersoids, which impede dislocation motion and retard microstructural coarsening, thereby improving the thermal stability and high-temperature performance of Al alloys[10,13]. On the other hand, regulating the precipitate/matrix interface structure through interface engineering and solute segregation can also suppress the coarsening of metastable precipitates to a certain extent, improving the thermal stability of the alloys[14,15]. For Al-Cu-Mn based heat-resistant systems, recent studies have shown that substituting traditional metastable strengthening phases with thermally stable equilibrium phases is an effective strategy to enhance the high-temperature strength at 300 °C. For example, exclusive strengthening by the T phase ($Al_{20}Cu_2Mn_3$) can significantly improve the medium-to-high-temperature tensile properties[9]. Meanwhile, solution and aging parameters exert a decisive influence on precipitation behavior, phase stability, and the strengthening effect. Rationally designing the heat treatment window is crucial for fully exploiting the high-temperature strengthening potential of alloys[12,16,17]. However, due to issues involving multi-component coupling, the sensitivity of process parameters, and complex microstructural evolution in heat-resistant cast aluminum alloys, the traditional research and development paradigm relying on experience and trial-and-error often entails long cycles and high costs, making it difficult to rapidly identify globally optimal solutions within the vast composition-process space[18].

In recent years, data-driven machine learning methods have demonstrated significant advantages in the fields of material composition design, process optimization, and performance prediction[19-21]. By learning the complex nonlinear relationships among composition, processing, microstructure, and properties from existing experimental data, machine learning can significantly enhance the efficiency of new material development and reduce experimental costs[19,20,22,23]. Furthermore, the development of active learning, explainable machine learning, and automated machine learning has enabled data-driven methods to exhibit stronger capabilities in sparse data modeling, multi-objective optimization, and key feature identification[24-27]. This indicates that machine learning is particularly suitable for complex systems like heat-resistant cast aluminum alloys, which possess high-dimensional compositional spaces and strong

nonlinear composition-process-property coupling relationships. However, compared to its rapid development in high-entropy alloys and other structural materials, the application of machine learning in the synergistic optimization of composition and processes for heat-resistant cast aluminum alloys remains relatively limited, especially lacking targeted design research oriented toward high-temperature tensile properties[21,26-29].

Based on this, the present study proposes a data-driven integrated design strategy to enhance the tensile strength of heat-resistant cast aluminum alloys. First, a database encompassing testing conditions, alloy compositions, process parameters, and physicochemical features was constructed based on high-quality experimental data from literature. Subsequently, a machine learning prediction model was established to predict high-temperature tensile properties, and it was coupled with a genetic algorithm to perform global optimization of the composition and heat treatment process parameters. On this basis, four novel heat-resistant cast aluminum alloys were designed and fabricated for experimental validation. Further, the microstructural features and high-temperature strengthening mechanisms were systematically analyzed, and a quantitative correlation among composition, processing, microstructure, and properties was established. This study provides new research perspectives and methodological support for the rapid development of high-performance heat-resistant cast aluminum alloys.

RESEARCH METHODS

Strategy and method of alloy composition design

This study proposes an interpretable machine learning-assisted co-design strategy for heat-resistant cast aluminum alloys, with its overall workflow illustrated in Figure 1. Implemented on the Python Scikit-learn platform[30], this framework primarily consists of six phases: data collection, feature construction and selection, model training and evaluation, genetic algorithm optimization, SHAP interpretability analysis, and experimental validation. First, a foundational database is constructed by collecting data on alloy compositions, processing parameters, testing conditions, and ultimate tensile strength (UTS) of heat-resistant cast aluminum alloys from published literature. Subsequently, a descriptor set reflecting the physicochemical characteristics of the elements is constructed by combining alloy compositions with intrinsic elemental

properties. To effectively reduce the dimensionality of the alloy design variables, a machine learning model is built using the selected features as inputs and UTS as the output, with its performance evaluated by the coefficient of determination (R^2). Building upon this, a genetic algorithm is coupled to co-design novel alloy compositions and heat treatment parameters. The SHAP interpretability method is then employed to quantitatively reveal the contribution of each key feature to the UTS. Finally, experimental fabrication and performance testing are conducted to validate the UTS of the designed alloys at 300 °C, and their heat-resistant strengthening mechanisms are systematically elucidated in conjunction with microstructural characterization.

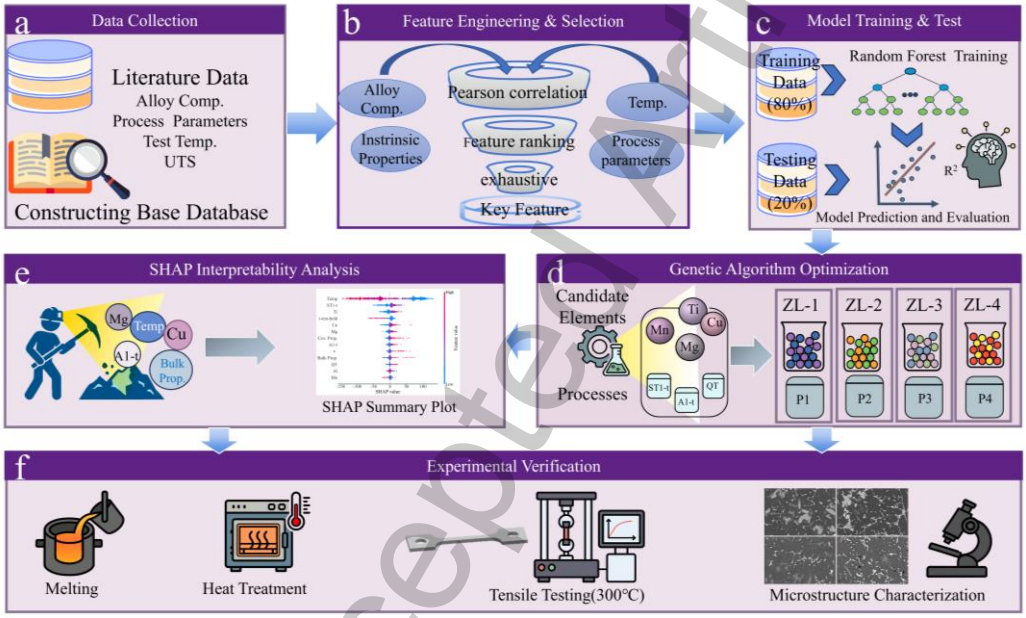

Figure 1. Schematic workflow of the interpretable machine-learning-assisted composition-process co-design strategy for heat-resistant cast aluminum alloys: (a) data collection and database construction; (b) feature engineering and key-feature selection; (c) model training, testing, and performance evaluation; (d) genetic-algorithm-based optimization of alloy compositions and processing parameters; (e) SHAP-based model interpretation; and (f) experimental validation, including alloy preparation, heat treatment, elevated-temperature tensile testing, and microstructural characterization.

Data collection

A total of 1,298 sets of "composition-testing conditions-heat treatment parameters-UTS" data for heat-resistant cast aluminum alloys were collected from published

literature, as detailed in Supplementary Information 1. To minimize the impact of processing variations on the consistency of the alloy performance data, only specimens subjected to the identical processing route-namely, casting → solution treatment → aging-were selected during the data collection process.

Calculation of features

A dataset of elemental physical properties was collected from standard handbooks. For each alloying element, 50 intrinsic attributes were compiled to construct the elemental feature vectors, including atomic number, atomic weight, lattice parameters, atomic radius, electronegativity, Young's modulus, among others. The names and numerical values of these physicochemical properties are provided in Supplementary Information 2. To quantitatively describe the relationship between alloy composition and mechanical performance, composition-related features were constructed based on the physicochemical properties of alloying elements. Considering an alloy composed of n elements, the compositional fraction of the i-th element is denoted as c_i, and its k-th elemental property is denoted as a_{ik}, where $k = 1,2,\dots,m$ represents different types of elemental properties. For a given elemental property, the equivalent alloy-level feature was defined using a composition-weighted average, as expressed in Eq. (1):

$$\bar{A}_k = \sum_{i=1}^{n} c_i \, a_{ik} \tag{1}$$

where $\bar{A}_k$ represents the average alloy feature corresponding to the k-th elemental property. Using Eq. (1), 50 physicochemical feature values were calculated for each alloy sample. By combining these 50 features with alloy composition variables and experimental processing parameters, a total of 105 features were constructed.

Feature selection and model construction

To efficiently identify the key features influencing the ultimate tensile strength (UTS), a hybrid feature selection strategy was employed by integrating linear correlation screening, random forest feature importance ranking, and exhaustive calculation. The specific procedures are described as follows.

Step 1: Pearson correlation-based feature screening. The Pearson correlation coefficient r between any two features x and y was calculated according to Eq. (2):

$$r = \frac{\sum_{i=1}^{n}(x_i - \bar{x})\,(y_i - \bar{y})}{\sqrt{\sum_{i=1}^{n}(x_i - \bar{x})^2}\,\sqrt{\sum_{i=1}^{n}(y_i - \bar{y})^2}} \tag{2}$$

where x_i and y_i represent the values of features x and y, respectively, for the i-th sample; n is the total number of samples; and $\bar{x}$ and $\bar{y}$ are the corresponding mean values calculated over the entire dataset. When $|r| > 0.7$, the two features were considered strongly correlated, indicating potential redundancy; thus, one of the correlated features was removed. The primary objective of correlation-based screening was to retain features with significant relevance to the prediction target while minimizing redundant or irrelevant variables.

Step 2: Random forest feature importance ranking. A random forest algorithm, which is well suited for high-dimensional datasets and exhibits strong predictive performance and robustness against overfitting, was employed to evaluate and rank feature importance. Based on the importance scores, the top 15 features were retained for subsequent analysis.

Step 3: Exhaustive calculation. Exhaustive calculations were performed on the top 15 features that exhibited no strong mutual correlations. Feature combinations yielding the highest prediction accuracy were selected as the final key features. During model construction, the dataset was randomly divided into training and test sets with a ratio of 4:1. The training set was used to establish the exhaustive calculation models, and 10-fold cross-validation was employed to evaluate the generalization capability and stability of the models. A random forest regression algorithm implemented in Scikit-learn was used to construct the UTS prediction model. Model accuracy was evaluated using the coefficient of determination R^2 for both the training and test datasets, as defined in Eq. (3):

$$R^2 = 1 - \frac{\sum_{i=1}^{n}(y_i - \hat{y}_i)^2}{\sum_{i=1}^{n}(y_i - \bar{y})^2} \tag{3}$$

where y_i is the experimental value, $\hat{y}_i$ is the model-predicted value, and $\bar{y}$ is the mean of the experimental values. The numerator represents the residual sum of squares (RSS), while the denominator represents the total sum of squares (TSS). A higher R^2 value indicates better agreement between predictions and experimental data. Based on the R^2 values obtained from exhaustive calculations, the key features governing UTS were identified.

To evaluate the robustness and predictive uncertainty of the model, 10-fold cross-validation was further performed on the training set. The mean value and standard deviation of the cross-validation R^2 were calculated. In addition, a residual-based 95% prediction interval was estimated from the residuals between the experimental UTS values and the corresponding out-of-fold cross-validation predictions.

Alloy design

Based on the UTS prediction model established in Section *Feature selection and model construction*, a genetic algorithm was employed to maximize the UTS. In this optimization process, alloy compositions and processing parameters were simultaneously treated as decision variables. To mitigate the risk of convergence to local optima in the high-dimensional design space, a deep heuristic search strategy was adopted, with a population size of 5000 and 5000 evolutionary generations. This high-density sampling strategy (a total of 2.5×10^7 evaluations) ensured effective global exploration of the design space. Ultimately, four candidate alloy compositions were selected from the optimization results for experimental validation.

SHAP analysis

To quantitatively interpret the model predictions and reveal the complex nonlinear relationships embedded within the machine learning "black-box" model, the SHapley Additive exPlanations (SHAP) method based on cooperative game theory was employed[31]. The core concept of SHAP lies in the computation of Shapley values, which allocate feature importance by evaluating the average marginal contribution of a feature across all possible feature coalitions. For feature i, the SHAP value is defined as:

$$\emptyset_i(f) = \sum_{S \subseteq N \backslash \{i\}} \frac{|S|!\,(|N| - |S| - 1)!}{|N|!} [f(S \cup \{i\}) - f(S)] \quad (4)$$

where N denotes the set of all input features, and S represents a subset of features that does not include feature i ($S \subseteq N \backslash \{i\}$). The terms $f(S)$ and $f(S \cup \{i\})$ correspond to the model predictions using feature subsets S and $S \cup \{i\}$, respectively. The weighting factor $\frac{|S|!(|N| - |S| - 1)!}{|N|!}$ accounts for all possible permutations of feature subsets. By computing these weighted marginal contributions, the SHAP framework provides a consistent and quantitative interpretation of feature importance, thereby elucidating the specific strengthening contributions of key alloying elements and processing parameters to the UTS.

Experimental method

Alloy preparation

Commercially pure aluminum (>99.7 wt.%), commercially pure magnesium (99.97 wt.%), and Al-50Cu, Al-10Mn, and Al-10Ti master alloys were utilized as raw materials. The experiments employed a conventional gravity casting process. The raw materials were melted and maintained at 720 °C, and subsequently poured into a metallic mold preheated to 250 °C (held for 2 hours prior to pouring). For comparative study, high-performance commercial alloy grades ZL114A (Al-6.92Si-0.26Fe-0.58Mg-0.12Ti-0.014Cu-0.078Mn, wt.%) and ZL205A (Al-4.87Cu-0.506Mn-0.27Ti-0.16Gd-0.12V-0.15Zr, wt.%) were selected, and control specimens were fabricated using the identical process described above. Rectangular specimens with dimensions of 75 × 20 × 20 mm were sectioned from the ingots for subsequent processing. The heat treatment protocol for the designed alloys comprised a solution treatment at 510 °C followed by an aging treatment at 165 °C. The heat treatments for the commercial alloys were executed in accordance with references[32,33].

Microstructure characterization and mechanical properties

Microstructural evolution and phase distribution were characterized using a scanning electron microscope equipped with an energy-dispersive spectrometer (SEM-EDS, JSM-7001F, JEOL, Tokyo, Japan). Cubic specimens with dimensions of 10 × 10 × 10 mm^3 were cut from the heat-treated ingots. Prior to observation, the specimen surfaces

were mechanically ground and polished, followed by etching with Keller's reagent (5 mL HNO_3, 3 ml HCL, 2 ml HF, and 190 mL distilled water) for 3-5 s. Phase identification was performed using X-ray diffraction (XRD, MiniFlex 600, Rigaku, Tokyo, Japan) over a 2θ range of 10°-90°, with a step size of 0.01° and a scanning rate of 5° min^{-1}. Secondary dendrite arm spacing (SDAS) was measured from optical micrographs using the line-intercept method and ImageJ software. At least five micrographs per alloy were analyzed, and the results are reported as average ± standard deviation to assess dendritic refinement and solidification characteristics.

Precipitate nanostructure and interfacial features in the ZL-2 alloy were characterized by transmission electron microscopy (TEM). TEM foils were prepared by mechanical grinding and ion milling (Gatan 691 PIPS, USA) to electron transparency. TEM, high-resolution TEM (HRTEM), scanning transmission electron microscopy (STEM), and STEM-energy-dispersive X-ray spectroscopy (STEM-EDS) were performed on a Talos F200X microscope (Thermo Scientific, USA) at 200 kV. Fast Fourier transform (FFT) and inverse FFT analyses of HRTEM images were conducted using DigitalMicrograph. Precipitate sizes were measured from representative TEM images with ImageJ, and the average size and standard deviation were calculated.

High-temperature tensile tests at 300 °C were conducted using a universal testing machine equipped with a high-temperature furnace (E45.305, 200 kN, MTS). Tensile specimens were machined from the heat-treated blocks according to the dimensions shown in Figure 2. The specimens were polished to eliminate potential stress concentrations introduced by wire electrical discharge machining (wire-EDM). All tests were carried out in accordance with the GB/T 4338-2006 standard. A preload of 50 N was applied, and the tensile rate v was set to 0.06 mm/min. To ensure thermal equilibrium, the specimens were held at the target temperature for 60 min prior to loading. Three independent tensile tests were conducted for each alloy, and the results are reported as mean ± standard deviation.

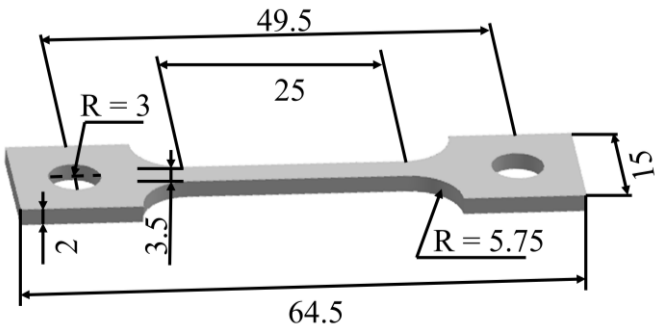

Figure 2. Schematic illustration of the tensile specimen dimensions (unit: mm).

RESULTS AND DISCUSSION

Property datasets and data distribution

Figure 3a illustrates the distribution of alloy compositional complexity within the UTS dataset. The samples predominantly consist of multicomponent systems, ranging from ternary alloys to complex combinations containing up to 12 elements. This high degree of compositional diversity, coupled with the intricate combinations of alloying elements, significantly expands the informational landscape of the dataset. While this enhances the generalization capability of machine learning models for complex multicomponent systems, it simultaneously exacerbates the challenges associated with alloy optimization and mechanical property tailoring.

The dataset encompasses 32 distinct alloying elements, with their specific types and compositional distributions detailed in Figure 3b. Notably, La exhibits the broadest compositional range among the additions (0-19.38 wt.%), while the maximum contents of Si, Ce, Mg, Cu, and Ni all exceed 5 wt.%. Elements such as Mn, Er, Fe, Cr, and Zn are primarily distributed within the 1.0-5 wt.% range, whereas the remaining elements are largely concentrated below 1 wt.%. Guided by these distributions, the compositional search space was strategically defined to align with practical content ranges, thereby improving modeling efficiency and mitigating the computational burden of high-dimensional feature spaces.

Figure 3c presents the distribution of processing parameters. The dataset covers a broad spectrum of critical variables, including melting conditions, heat-treatment parameters (solution and aging temperatures/times), and tensile testing conditions. These parameters exhibit distinct distributions with wide spans, reflecting the diverse

fabrication routes reported in the literature. Such extensive coverage facilitates the model's ability to learn complex composition-process-property relationships, although it inevitably increases the dimensionality and nonlinearity of the feature space.

The distribution of UTS values with respect to testing temperature is shown in Figure 3d. The UTS ranges from 11 to 590 MPa across testing temperatures of 20-530 °C. Data collected at 25 °C constitute the largest fraction (~ 33.9%), with significant portions also at 250 °C, 300 °C, and 350 °C. Conversely, samples at other temperatures account for less than 10%. This distribution indicates that existing research has focused primarily on room and elevated temperatures, while data at the extremities of this temperature spectrum remain relatively scarce.

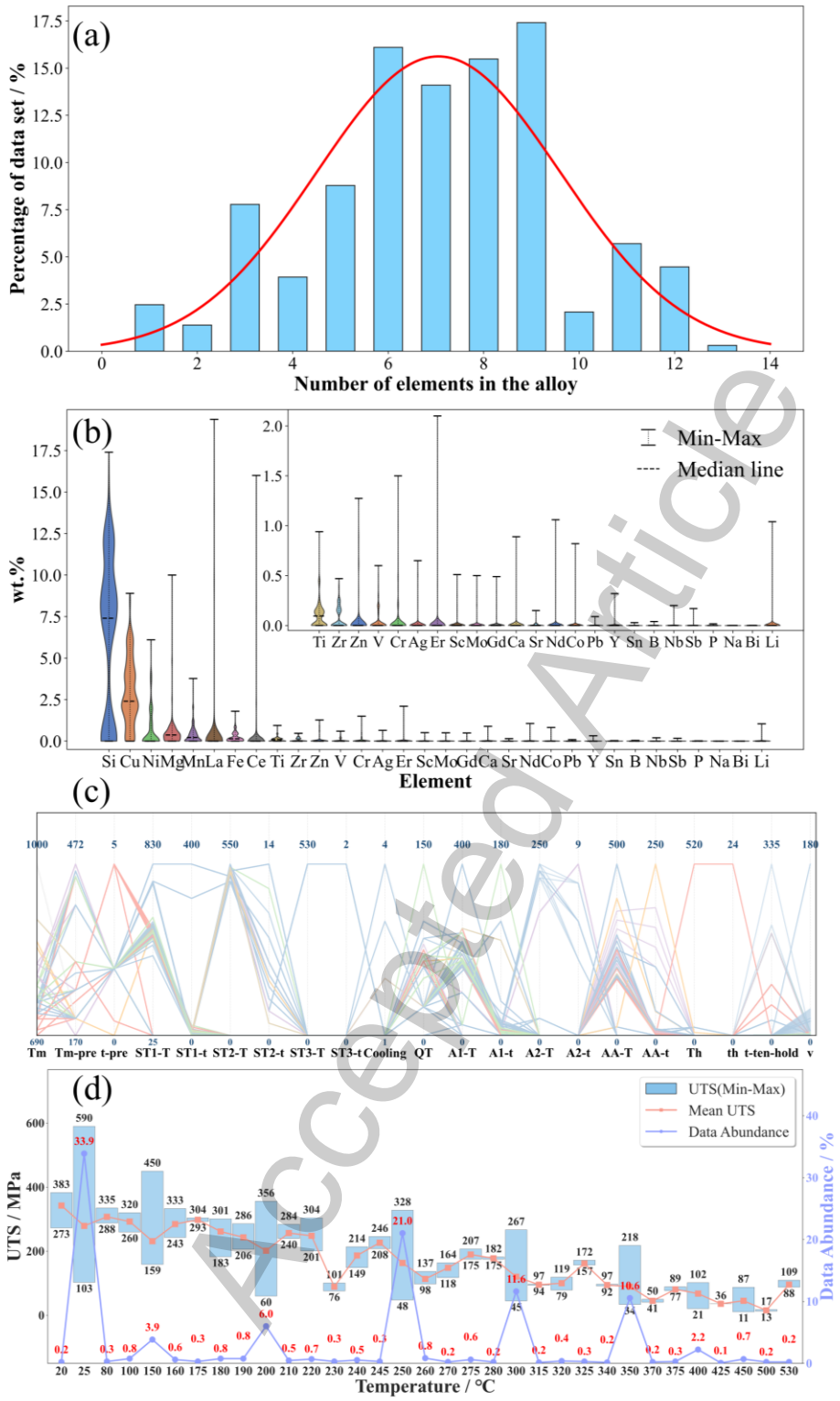

Figure 3. Comprehensive statistical overview of the alloy dataset, covering compositional, processing, and mechanical property spaces. (a) Distribution of the number of constituent elements per alloy system. (b) Statistical distribution of elemental concentrations (wt.%) across the dataset, with an inset highlighting minor alloy addition. (c) Types and value distributions of processing parameters included in

the dataset. (d) Temperature-dependent ultimate tensile strength (UTS) statistics, showing data abundance, mean trends, and min-max variations.

Feature selection and prediction models of properties

First, the Pearson correlation coefficient was employed to screen the initial feature set and eliminate multicollinearity between variables. Figure 4a presents the feature correlation heatmap after removing strongly correlated variables. This step ensures the independence of input variables, thereby reducing model redundancy and enhancing computational efficiency. Subsequently, feature contribution was evaluated based on the Random Forest (RF) algorithm, with the top 15 features by importance score shown in Figure 4b. The results indicate that the testing temperature (Temp) has a decisive influence on the ultimate tensile strength (UTS) of the alloy. Furthermore, the thermal exposure time before high-temperature tension (t-ten-hold) and the primary aging time (A1-t) also exhibited high importance. This reflects the significant impact of matrix recovery and precipitate coarsening-induced by holding time at elevated-temperatures on strength evolution. Given the compositional framework and service conditions of heat-resistant cast aluminum alloys, the Al content and testing temperature (Temp) were initialized as the baseline input features for the model. To determine the optimal feature subset, an exhaustive feature selection strategy was adopted, using the coefficient of determination (R^2) from 10-fold cross-validation as the evaluation metric. As illustrated in Figure 4c, the model performance rises rapidly with the number of features before reaching a plateau. The performance peaks at 13 features (indicated by the red star). In Figure 4b, the pink bars represent the feature subset selected for the optimal model, while the blue bars represent excluded features whose inclusion would increase model complexity without significantly improving generalization capability. The UTS prediction results based on this optimal feature set are shown in Figure 4d. The experimental measurements and model predictions demonstrate high consistency, with R^2 values for the training and testing sets reaching 0.885 and 0.881, respectively. Additionally, the Mean Absolute Error (MAE) for the testing set is 22.639 MPa, indicating that the model accurately captures the complex nonlinear mapping between temperature, composition, processing, physicochemical properties, and tensile strength. To further quantify the robustness of the model, 10-fold cross-validation was performed on the training set. The average cross-validation R^2 was 0.885 with a standard deviation of 0.023, indicating stable predictive performance across different data partitions. The

independent test set yielded an R^2 of 0.881, an RMSE of 32.944 MPa, and an MAE of 22.639 MPa. Furthermore, the residual-based 95% prediction interval was estimated from the cross-validation residuals. The 2.5th and 97.5th percentiles of the residuals were −68.207 MPa and 75.926 MPa, respectively. Therefore, for a predicted UTS value $\hat{y}$, the empirical 95% prediction interval can be expressed as $\hat{y} - 68.207$ MPa to $\hat{y} + 75.926$ MPa. In addition, a benchmark comparison among ten representative regression algorithms was performed using the same feature subset and data partitioning, as summarized in Supplementary Information 3. RF exhibited the best overall balance among predictive accuracy, robustness, and generalization capability; therefore, it was selected as the final model.

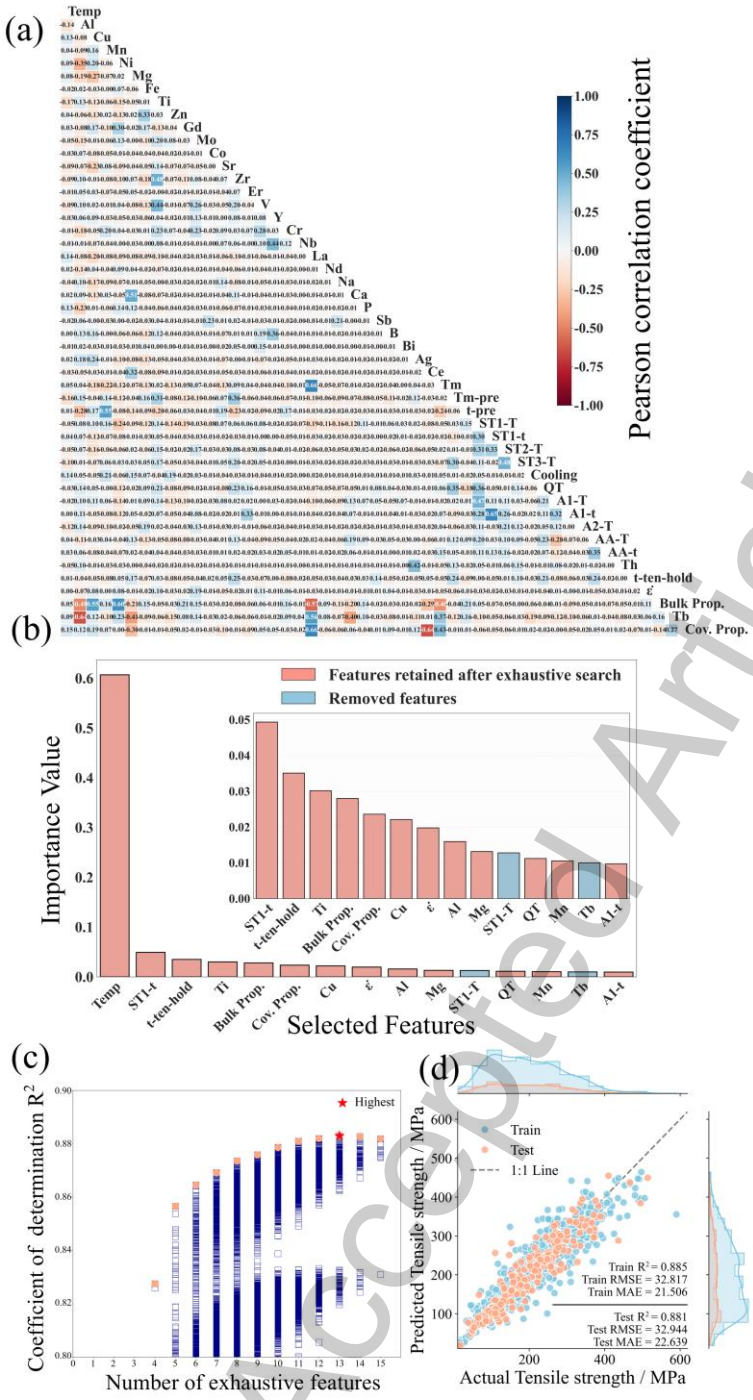

Figure 4. Feature screening procedure and results of feature selection. (a) Pearson correlation coefficients of the candidate features after eliminating strongly correlated variables, (b) Importance ranking of the top 15 selected features, where the blue bars indicate features removed during the exhaustive feature selection process, (c) Exhaustive feature selection results showing the variation of model performance (10-fold cross-validated R^2) with the number of selected features, (d) Comparison between predicted and experimentally measured tensile strength for the optimal model.

Machine learning-assisted alloy design

Based on the established UTS prediction model, a co-design optimization of alloy compositions and processing parameters was performed. For the compositional design, Al was used as the matrix element, with four candidate alloying elements (Cu, Mg, Mn, and Ti) serving as design variables. To ensure physical consistency and data integrity, the sum of the mass fractions of these five elements was strictly constrained to 100%. On this basis, three heat treatment parameters (solution time ST1-t, artificial aging time A1-t, quenching temperature QT), three testing conditions (tensile temperature Temp, thermal exposure time t-ten-hold, tensile rate v), and two types of physicochemical descriptors (bulk modulus Bulk Prop. and covalent radius Cov. Prop.) were combined to systematically explore optimal combinations. The tensile rate was fixed at 0.06 mm/min. Given that the typical service temperature for piston alloys is approximately 300 °C [34], the design temperature (Temp) was set accordingly to ensure alignment with actual engineering service conditions. Simultaneously, the thermal exposure time (t-ten-hold) was unified at 60 min. This setting is a widely adopted standard in high-temperature mechanical testing to minimize interference from transient thermal gradients and short-term microstructural instability, thereby improving the reliability and comparability of the model-guided UTS data. Physicochemical descriptors were dynamically calculated according to the method described in Section *Calculation of features*. The compositional search boundaries were defined according to the elemental concentration ranges covered by the experimental database, ensuring that GA optimization was performed within the data-supported domain of the trained ML model and avoiding unreliable extrapolation. Practical metallurgical constraints were also considered, since excessive alloying contents may promote microsegregation, coarse brittle intermetallic formation, hot tearing, and casting defects, thereby deteriorating castability and heat-treatment response. The specific search ranges and constraints for alloy compositions and heat treatment parameters are listed in Table 1, defining the boundary conditions for the genetic algorithm (GA) optimization. Based on the GA optimization results, four alloys (labeled ZL-1, ZL-2, ZL-3, and ZL-4) were selected for experimental validation, with their compositions, processing parameters, and predicted performance summarized in Table 2.

As shown in Table 2, the absolute relative deviations between the predicted and experimental UTS values of the four designed alloys are 3.08%, 8.96%, 12.92%, and

0.46%, respectively, with an average deviation of 6.36%. These results indicate that the machine learning model can reasonably capture the general strength level of the designed alloys, although certain deviations remain. It should also be noted that the predicted UTS values are slightly lower than the corresponding experimental values for all four alloys, suggesting a certain degree of systematic underestimation. This discrepancy may be attributed to several factors. First, unavoidable experimental uncertainties may be introduced during alloy melting, casting, heat treatment, and tensile testing. Second, the measured alloy compositions differ slightly from the nominal compositions used for model prediction, which may affect the final mechanical properties. Third, the current model mainly considers alloy compositions and processing parameters, while microstructural factors such as phase fraction, precipitate size, grain-boundary phase distribution, and defect characteristics were not explicitly included as input descriptors. Therefore, although the model provides useful guidance for alloy and process design, further incorporation of additional experimental data and quantitative microstructural descriptors is expected to improve the prediction accuracy and generalization capability of the model.

Table 1. The defined search space boundaries for alloy compositions and processing parameters employed in the genetic algorithm optimization

Search space	Cu	Mg	Ti	Mn	ST1-t	A1-t	QT (℃)
Lower limit	0	0	0	0	2	6	25
Upper limit	9	10	2	4	24	12	75
Step	0.01	0.01	0.01	0.01	2	2	50

Table 2. Nominal chemical compositions (wt.%) of the ZL-1~ZL-4 alloys, measured compositions listed in parentheses, heat-treatment parameters, and predicted and experimental UTS values with corresponding relative deviations

Alloy	Cu (wt.%)	Mg	Ti	Mn	Al	ST1-t (h)	A1-t (h)	QT (℃)	UTS (MPa) Pred.	Exp.	Relative deviation/%
ZL-1	3.62 (3.66)	3.00 (3.48)	1.92 (1.98)	1.35 (1.43)	Bal.	2	12	75	176	181.6	3.08
ZL-2	5.96 (6.17)	2.9 (3.40)	0.42 (0.38)	1.35 (1.46)	Bal.	4	12	75	195	214.2	8.96

ZL-3	3.43 (3.58)	3.00 (3.48)	0.63 (0.56)	1.43 (1.54)	Bal.	8	12	75	178.6	205.1	12.92
ZL-4	4.86 (4.69)	2.88 (3.38)	0.33 (0.31)	1.39 (1.64)	Bal.	16	12	75	194	194.9	0.46

High-temperature mechanical properties

The tensile properties of the designed alloys were experimentally tested at 300 °C and compared with two commercial cast aluminum alloys, ZL114A and ZL205A, as shown in Figure 5. The experimental results indicate that the machine learning-designed alloys significantly outperform the commercial alloys in terms of elevated-temperature strength. Among them, the ZL-2 alloy exhibits the highest ultimate tensile strength (UTS), reaching 214.2 MPa. Compared to ZL114A (133.0 MPa) and ZL205A (171.2 MPa), its strength increased by 61.0% and 25.1%, respectively. The ZL-3 and ZL-4 alloys also demonstrate excellent elevated-temperature strength, with UTS values of 205.1 MPa and 194.9 MPa, respectively. In contrast, the tensile strength of the ZL-1 alloy is slightly lower at 181.6 MPa, which is primarily attributed to the presence of coarse primary intermetallic compounds within its microstructure.

To further benchmark the elevated-temperature tensile performance of the designed alloys, the UTS values at 300 °C were compared with those of previously reported heat-resistant cast aluminum alloys [35-41], as summarized in Table 3. The present ML-designed gravity-cast alloys exhibit UTS values ranging from 181.6 to 214.2 MPa at 300 °C, which are higher than those of the representative gravity-cast heat-resistant aluminum alloys listed in the table. In particular, the ZL-2 alloy achieves a UTS of 214.2 MPa, exceeding not only the commercial cast aluminum alloys examined in this study but also the previously reported gravity-cast alloys tested at the same temperature. It is noteworthy that several squeeze-cast alloys were also included as broader benchmarks, because squeeze casting generally provides improved densification and is often beneficial for mechanical performance compared with conventional gravity casting. Even under this broader comparison, the UTS values of the present gravity-cast alloys remain higher than those of the listed squeeze-cast alloys. This result highlights the effectiveness of the ML-guided composition-process co-design strategy in developing heat-resistant cast aluminum alloys with superior elevated-temperature

strength.

Regarding tensile ductility, traditional perspectives suggest that the introduction of thermally stable strengthening phases inevitably sacrifices material ductility, thereby leading to the typical strength-ductility trade-off[42-46]. However, the alloys designed in this study maintain a certain degree of ductility while preserving high strength. Specifically, the elongation of the ZL-3 alloy is approximately 4.18%, which is higher than that of the commercial cast alloys. These results demonstrate that the machine learning-assisted design strategy is capable of significantly enhancing elevated-temperature strength while some compositions retain comparatively favorable ductility.

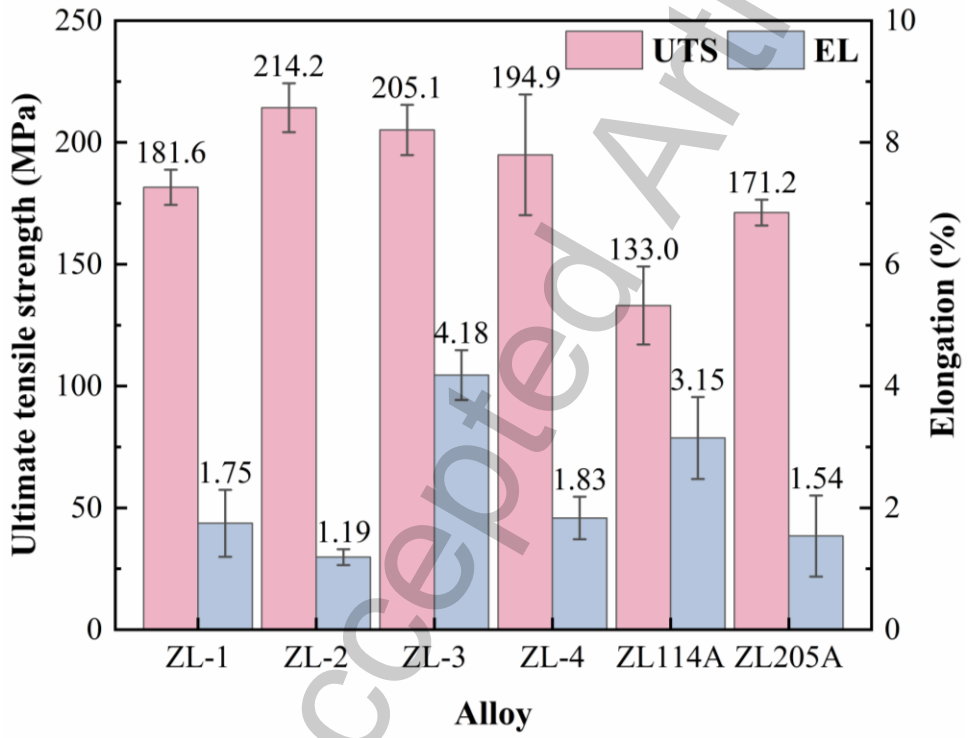

Figure 5. Elevated-temperature ultimate tensile strength (UTS) and elongation of the investigated alloys tested at 300 °C. The data are presented as the mean ± standard deviation (SD) of three replicate tensile tests for each alloy (n = 3).

Table 3. Ultimate tensile strength of the present alloys and previously reported heat-resistant cast aluminum alloys at 300 °C

Alloy composition, wt.%	Condition	UTS at 300 ℃	Reference

		(MPa)	
Al-3.66Cu-3.48Mg-1.98Ti-1.43Mn	T6, GC	181.6	This study
Al-6.17Cu-3.40Mg-0.38Ti-1.46Mn	T6, GC	214.2	This study
Al-3.58Cu-3.48Mg-0.56Ti-1.54Mn	T6, GC	205.1	This study
Al-4.69Cu-3.38Mg-0.31Ti-1.64Mn	T6, GC	194.9	This study
Al-12.41Si-4.19Cu-1.60Mn-0.0253Sr-0.5La	T6, GC	128.2	[35]
Al-12.24Si-4.09Cu-1.57Mn-0.0262Sr-0.5Ce	T6, GC	125.2	[35]
Al-4.7Cu-0.99Mn-0.0009Mg-0.097Fe-0.49Ni	T4, GC	119	[36]
Al-4.7Cu-0.99Mn-0.0009Mg-0.097Fe-0.49Ni	T6, GC	141	[36]
Al-4Cu-0.03Sb-0.206Mn-0.113Fe-0.05Si	T5, GC	139	[37]
Al-11.08Si-4.12Cu-0.19Fe-0.03Mn-0.2Zr-0.02Sr	T6, GC	115	[38]
Al-4.54Cu-0.917Mn-0.059Si-0.0004Mg-0.131Fe	T6, GC	116	[39]
Al-0.19Si-0.9Fe-2.5Cu-0.03Mn-1.6Mg-0.9Ni	T6, SC	132	[40]
Al-5.0Cu-0.6Mn-1.0Fe-0.5Ni	T7, SC	136	[41]
Al-5.0Cu-0.6Mn-1.0Fe-1.5Ni	T7, SC	152	[41]

[a] GC: gravity casting; SC: squeeze casting;

Phase constitution and microstructural characteristics

Table 4 lists the SDAS values measured from the as-cast optical micrographs of the investigated alloys, and the corresponding representative micrographs are presented in Figure S2. The SDAS values of the ZL-1-ZL-4 alloys range from 21.24 to 27.02 μm, indicating relatively refined dendritic structures. Among them, ZL-2 exhibits the smallest SDAS, whereas ZL-3 shows the largest value within the ZL-1-ZL-4 alloy series. In comparison, ZL205A exhibits the largest SDAS among all the investigated alloys, corresponding to a coarser as-cast dendritic structure. These results demonstrate that the investigated alloys possess different as-cast solidification microstructures.

SDAS is a characteristic parameter reflecting local solidification kinetics, dendritic refinement, and solute redistribution during casting. A smaller SDAS generally corresponds to a shorter interdendritic diffusion distance and a more refined dendritic framework, which may alleviate local microsegregation and promote more homogeneous solute redistribution in the as-cast matrix and during subsequent heat treatment. Therefore, SDAS measurement provides quantitative support for describing the initial casting microstructure and solidification characteristics of the investigated alloys.

It should be emphasized that SDAS is not the sole factor governing the elevated-temperature strength, but rather provides an important microstructural indicator for evaluating the initial solidification condition prior to heat treatment and precipitation. The relatively small SDAS of ZL-2 suggests a refined dendritic framework and shortened solute redistribution distance, which may facilitate a more uniform distribution of alloying elements during post-solidification heat treatment and provide a favorable microstructural basis for the subsequent formation of heat-resistant $Al_{20}Cu_2Mn_3$/Al_2CuMg-containing phases and nanoscale precipitates. This is consistent with the superior UTS of ZL-2 at 300 °C. In contrast, ZL-3 still exhibits high elevated-temperature strength despite having the largest SDAS among the designed alloys, indicating that the final strength is not determined by SDAS alone but by the combined effects of solidification microstructure, precipitation behavior, secondary-phase constitution, and phase distribution. Thus, the SDAS analysis serves as a quantitative microstructural complement to the machine-learning-guided composition-process design rather than an independent strength criterion.

Figure 6 shows the XRD results for each alloy. It can be observed that the characteristic diffraction peaks of $Al_{20}Cu_2Mn_3$ and Al_2CuMg are detected in ZL-2, ZL-3, and ZL-4, whereas the primary precipitate phase in ZL-1 is Al_2CuMg. In addition, Al_3Ti is detected in both the designed alloys and ZL205A; in contrast, the primary second phase in ZL114A is Mg_2Si. Figure 7 presents the representative SEM microstructural morphologies of the alloys. The numbered markers in the figures correspond to the EDS analysis locations, and the relevant results are summarized in Table 5. Combining the XRD and EDS analyses, the intermetallic compounds identified in the alloys primarily include $Al_{20}Cu_2Mn_3$, Al_2CuMg, Al_3Ti, Mg_2Si, primary Si, and eutectic Si.

As shown in Figure 7a, Al_3Ti in ZL-1 is mainly distributed intragranularly in a blocky or lath-like morphology, while Al_2CuMg predominantly precipitates at the grain boundaries as a fine dispersed phase. Figure 7b reveals that a large amount of $Al_{20}Cu_2Mn_3$- and Al_2CuMg-containing secondary phases/intermetallic phases are distributed along the grain boundaries of ZL-2; correspondingly, $Al_{20}Cu_2Mn_3$ and Al_3Ti phases can also be observed intragranularly. Compared with Figure 7b, the phase composition of ZL-3 in Figure 7c is fundamentally consistent, but the amount of intragranular Al_3Ti phase significantly increases, whereas the precipitation of $Al_{20}Cu_2Mn_3$ and Al_2CuMg at the grain boundaries decreases. ZL-4, shown in Figure 7d, exhibits an opposite trend: the amount of intragranular Al_3Ti phase decreases, while the precipitation of $Al_{20}Cu_2Mn_3$ and Al_2CuMg phases at the grain boundaries increases. In contrast, ZL114A in Figure 7e contains a large amount of Si-rich phases distributed continuously along the grain boundaries; while Figure 7f indicates that ZL205A mainly precipitates at the grain boundaries in the form of fine, discrete Al_3Ti particles.

As shown in Figure 8a, a high density of nanoscale precipitates is distributed in the Al matrix. The rod-like/plate-like precipitates in Figure 8b can be identified as Mn-rich $Al_{20}Cu_2Mn_3$ precipitates, as evidenced by the pronounced Mn and Cu enrichment in the corresponding STEM-EDS elemental maps. In contrast, the fine lath-like precipitates shown in Figure 8c are identified as Al_2CuMg precipitates, consistent with the enrichment of Cu and Mg. The corresponding indexed FFT patterns and lattice-fringe analyses are presented in Supplementary Figure S3. The HRTEM and inverse fast Fourier transform images in Figure 8b1 and b2 and Figure 8c1 and c2 further reveal clear lattice fringes within these precipitates and well-defined precipitate/matrix interfaces, indicating their crystalline nature and relatively favorable interfacial matching with the Al matrix. Such interfacial characteristics are beneficial for impeding dislocation motion and are expected to contribute to precipitation strengthening during elevated-temperature deformation. Statistical analysis shows that the average sizes of $Al_{20}Cu_2Mn_3$ and Al_2CuMg precipitates are 219.4 ± 119.0 nm and 109.8 ± 57.2 nm, respectively [Figure 8d and e]. Overall, two main types of nanoscale precipitates are observed in the ZL-2 alloy: relatively coarse rod-like/plate-like Mn-rich $Al_{20}Cu_2Mn_3$ precipitates and finer lath-like Al_2CuMg precipitates. The Mn-rich $Al_{20}Cu_2Mn_3$ precipitates are expected to provide thermally stable strengthening during elevated-temperature deformation, whereas the finer Al_2CuMg precipitates provide additional precipitation strengthening in the Al matrix. Therefore, the coexistence of these two

types of nanoscale precipitates contributes to the superior elevated-temperature strength of the ZL-2 alloy.

Previous studies have shown that the key to enhancing the elevated-temperature strength of cast heat-resistant aluminum alloys lies in suppressing dislocation climb and grain boundary atomic diffusion at high temperatures[47,48]. Complex intermetallic compounds distributed along grain boundaries can form relatively closed network-like or skeletal microstructures. Such microstructures facilitate the transfer of stress from the matrix to the strengthening phases and, to a certain extent, inhibit grain boundary sliding. Generally, the finer the second-phase particles and the more dispersed their distribution along the grain boundaries, the better the heat resistance of the alloy. It can be seen from Figure 7b that ZL-2 contains a relatively large amount of the $Al_{20}Cu_2Mn_3$ phase. $Al_{20}Cu_2Mn_3$ has been reported as a thermally stable Mn-rich strengthening phase in Al-Cu-Mn-based alloys, which can form during solidification and further precipitate as fine dispersoids during subsequent homogenization or solution treatment, thereby contributing to the enhanced thermal stability and elevated-temperature strength of Al alloys in the 300-350 °C range[49,50]. Therefore, the abundant and relatively stable $Al_{20}Cu_2Mn_3$ phases in ZL-2, together with the $Al_{20}Cu_2Mn_3$/Al_2CuMg composite structures distributed at the grain boundaries, can more effectively suppress dislocation climb and grain boundary sliding during elevated-temperature tensile testing, thereby exhibiting superior high-temperature strengthening effects. From Figure 7c and d, it can be further observed that the amount of intragranular Al_3Ti phases in ZL-3 increases, while the amount of $Al_{20}Cu_2Mn_3$ and Al_2CuMg phases at the grain boundaries decreases. This causes its strengthening effect to rely more on intragranular dispersed phases, resulting in a lower elevated-temperature strength compared to ZL-2. In ZL-4, the precipitation of $Al_{20}Cu_2Mn_3$ and Al_2CuMg at the grain boundaries increases, leading to enhanced grain boundary strengthening. However, due to the reduced amount of the intragranular Al_3Ti phase, the intragranular support is insufficient, and the overall strengthening effect still fails to reach the level of ZL-2. ZL-1, shown in Figure 7a, is predominantly composed of Al_2CuMg and lacks the more thermally stable $Al_{20}Cu_2Mn_3$ phase. Since strengthening phases related to the Al-Cu-Mg system are more prone to coarsening and strength degradation at high temperatures, its elevated-temperature performance is relatively weaker[51-53].

The microstructural characteristics of the commercial alloys are also consistent with the differences in their elevated-temperature performance. As shown in Figure 7e, a large number of Si-rich phases in ZL114A are continuously distributed along the grain boundaries. Such continuous grain boundary second phases weaken microstructural continuity. Moreover, its primary strengthening phase, Mg_2Si, easily coarsens and loses effectiveness above approximately 225 °C[54]; therefore, it is difficult to maintain a stable strengthening effect under 300 °C conditions. In contrast, the fine, discrete Al_3Ti particles precipitating at the grain boundaries of ZL205A in Figure 7f contribute to improving grain boundary stability[55,56]. However, due to the lack of a dominant heat-resistant phase with stronger thermal stability, its overall elevated-temperature strengthening effect remains limited. Overall, the elevated-temperature performance of the investigated alloys is governed by the coupled effects of the initial solidification microstructure, and the type, amount, morphology, and distribution of thermally stable secondary phases and nanoscale precipitates. This microstructural evidence supports the machine-learning-guided alloy design results, indicating that the superior UTS of ZL-2 at 300 °C arises from a favorable combination of refined solidification structure, stable $Al_{20}Cu_2Mn_3$/Al_2CuMg-containing phases, and nanoscale precipitation strengthening.

Table 4. SDAS values of the investigated alloys

Alloy	**ZL-1**	**ZL-2**	**ZL-3**	**ZL-4**	**ZL114A**	**ZL205A**
SDAS / μm	22.17±5.42	21.24±4.27	27.02±6.04	22.83±4.37	24.55 ±3.90	32.12±5.05

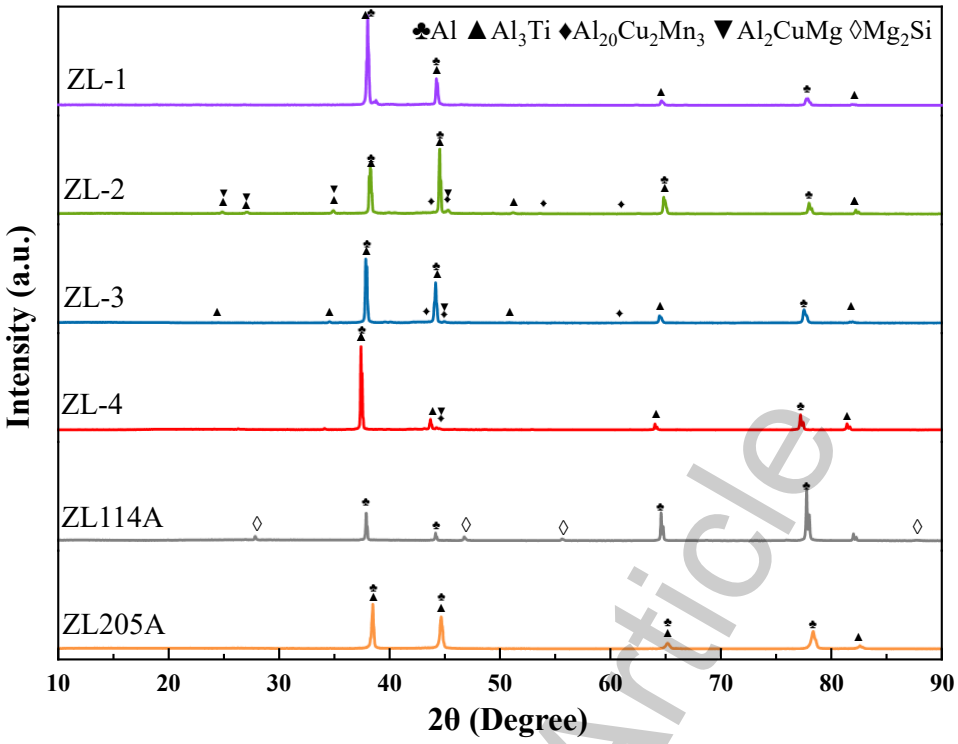

Figure 6. XRD patterns of the investigated alloys.

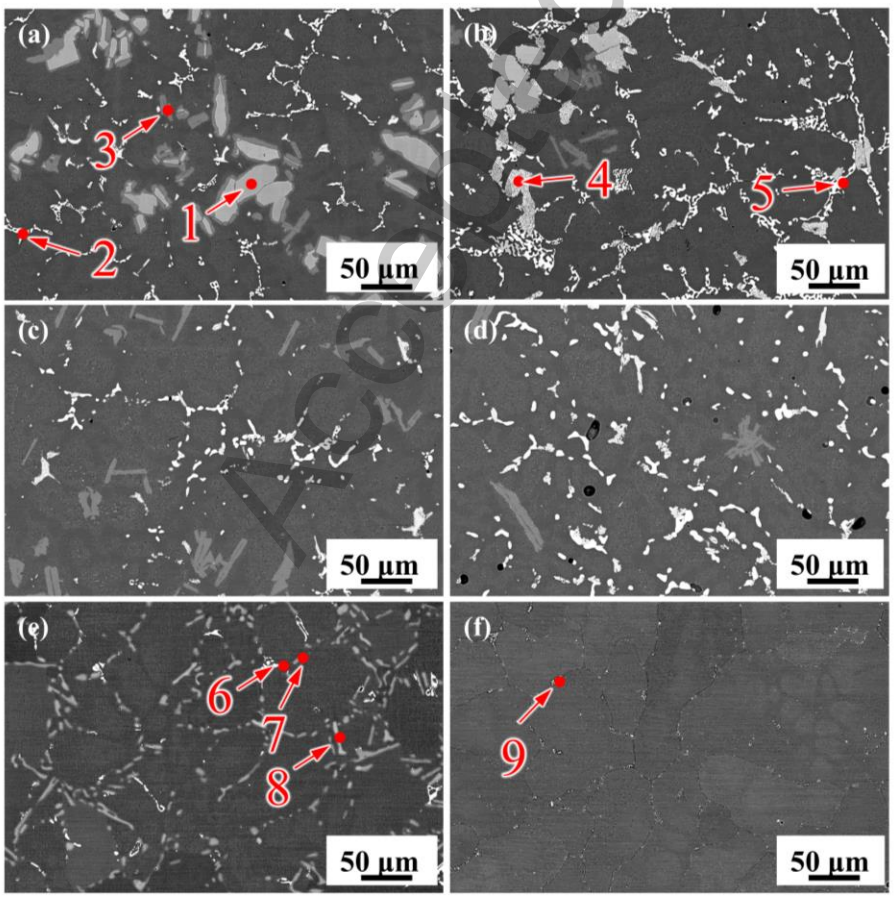

Figure 7. The microstructures of the alloys are as follows: (a) ZL-1, (b) ZL-2, (c) ZL-

3, (d) ZL-4, (e) ZL114A, (f) ZL205A.

Table 5. EDS analysis (at.%) at selected locations in Figure 7

Spot	Al	Cu	Mn	Mg	Ti	Si
1	74.77	0.03	-	-	25.2	-
2	66.94	16.58	0.06	16.4	0.01	-
3	78.58	0.3	0.32	12.46	8.34	-
4	77.71	8.7	13.23	0.35	0.01	-
5	57.45	22.26	0.16	20.13	-	-
6	55.42	-	0.39	15.54	-	28.66
7	38.06	-	-	0.18	0.02	61.73
8	63.72	-	-	0.35	-	35.93
9	86.23	2.27	0.93	-	10.4	-

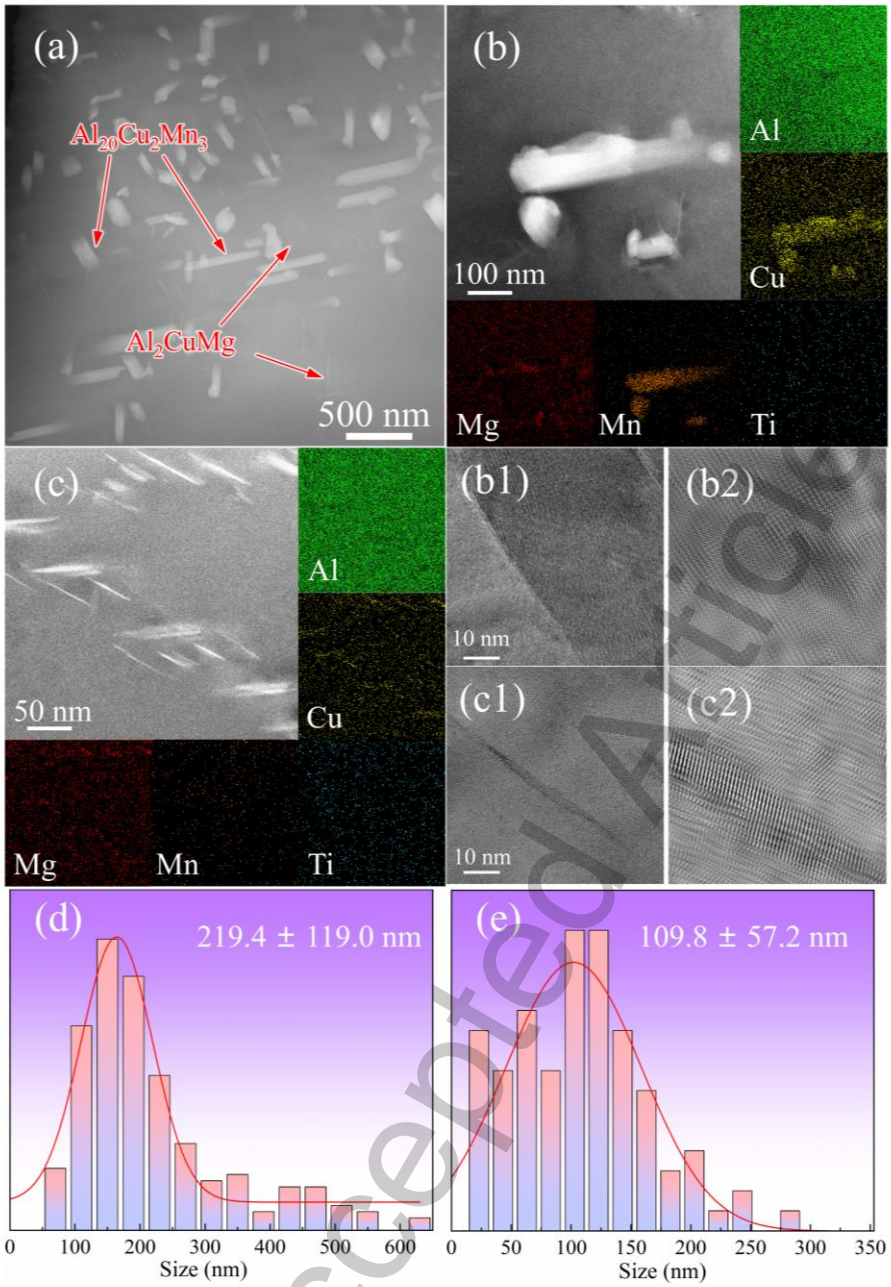

Figure 8. TEM characterization and size distribution of nanoscale precipitates in the ZL-2 alloy: (a) low-magnification TEM image; (b) STEM image and corresponding EDS elemental maps of Mn-rich $Al_{20}Cu_2Mn_3$ precipitates; (c) STEM image and corresponding EDS elemental maps of Al_2CuMg precipitates; (b1, b2) HRTEM and IFFT images of $Al_{20}Cu_2Mn_3$; (c1, c2) HRTEM and IFFT images of Al_2CuMg; (d, e) size distributions of $Al_{20}Cu_2Mn_3$ and Al_2CuMg precipitates, respectively.

Interpretability analysis of the machine learning model

Since the Random Forest model is a typical black-box model, relying solely on

prediction accuracy is insufficient to reveal the actual contributions of individual input variables to the ultimate tensile strength (UTS). Therefore, this study further employs the SHAP (SHapley Additive exPlanations) method to interpret the model. Figure 9 presents the SHAP bee swarm plot (summary plot), where each feature is ranked according to its mean absolute SHAP value to characterize its global impact magnitude on the UTS prediction. It can be observed that Temp (temperature) is the primary factor affecting UTS. The SHAP values corresponding to high temperatures are mainly distributed in the negative region, while low temperatures mostly correspond to positive contributions, indicating that elevated temperatures significantly suppress UTS. This result is highly consistent with the fundamental metallurgical principles of matrix softening, the activation of dislocation motion, and the enhancement of grain boundary sliding at high temperatures. In addition to temperature, ST1-t, Ti, t-ten-hold, Cu, and Mg also exhibit high feature importance, indicating that heat treatment parameters and key alloying elements jointly dominate the strength evolution. Particularly, the prominent roles of Cu, Mg, and Ti correspond to the primary strengthening phases such as $Al_{20}Cu_2Mn_3$, Al_2CuMg, and Al_3Ti identified in Section **Phase constitution and microstructural characteristics**. This demonstrates a strong consistency between the key features extracted by the machine learning model and the microstructural strengthening mechanisms revealed by experiments. To further analyze the effect of key compositional features, Figure 10 presents the SHAP dependence plot of Cu, colored by Mn and Mg contents, respectively. As seen in Figure 10a and b, the contribution of Cu to the UTS exhibits obvious nonlinear characteristics. At low Cu contents, its SHAP values are generally low or even negative; as the Cu content increases, the SHAP values gradually turn positive and increase significantly, indicating that higher Cu contents are more conducive to improving the UTS. This trend implies that the strengthening effect of Cu is not linearly cumulative, but rather closely related to its capability to participate in the formation of effective strengthening phases. Furthermore, Figure 10 also indicates that the effect of Cu is synergistically modulated by Mn and Mg. Combined with the analysis in Section **High-temperature mechanical properties**, Mn participates in the formation of the highly thermally stable $Al_{20}Cu_2Mn_3$ phase, while Mg co-forms the Al_2CuMg phase with Cu. Therefore, the interactions between Cu-Mn and Cu-Mg possess a clear microstructural basis; that is, the contribution of Cu to the strength depends not only on its intrinsic concentration but also on whether it can synergistically promote the precipitation and stable distribution

of heat-resistant strengthening phases. Among these, the synergistic effect of Cu-Mn is of vital significance for high-temperature strengthening because $Al_{20}Cu_2Mn_3$ possesses superior thermal stability, making it more effective at pinning and inhibiting dislocation climb and grain boundary sliding during high-temperature tensile deformation. Overall, the SHAP analysis indicates that the prediction of UTS by the Random Forest model primarily relies on temperature, heat treatment processes, and key compositional variables such as Cu, Mg, and Ti. Furthermore, these highly important features align well with the phase constituents and microstructural evolution patterns obtained via experimental characterization. These results demonstrate that the established model not only possesses excellent predictive capability but also reflects, to a considerable extent, the underlying materials science principles governing the variations in the high-temperature strength of the alloys.

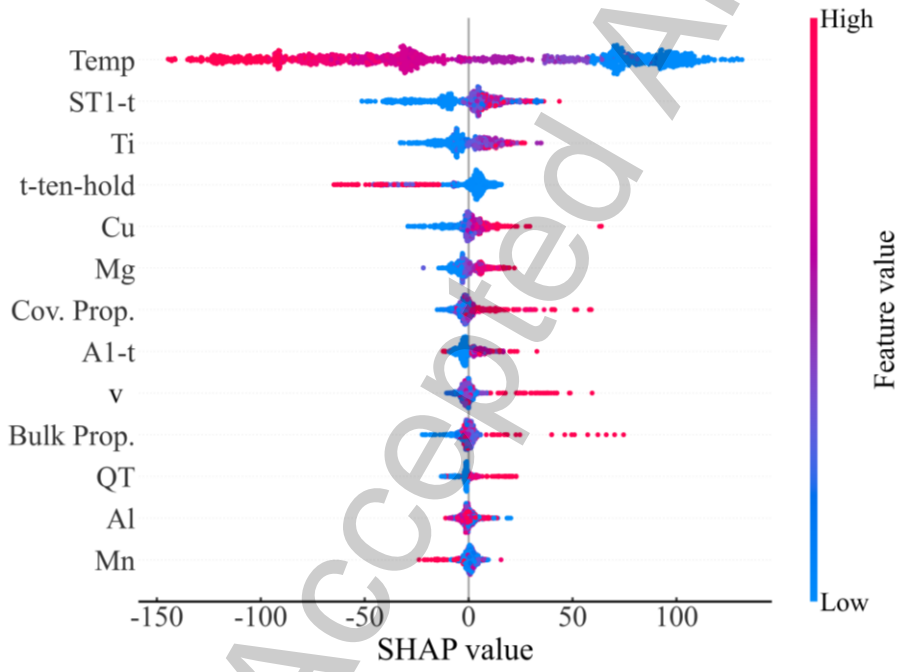

Figure 9. SHAP bee swarm plot (summary plot) obtained from the trained Random Forest model. Each dot represents a sample in the dataset. The horizontal axis represents the corresponding SHAP value of the feature, where positive and negative values indicate positive and negative contributions to the UTS, respectively, and the absolute value reflects the magnitude of the contribution. The color of the dots represents the normalized feature value (blue for low values, red for high values). Features are ranked from top to bottom according to their mean absolute SHAP values (mean|SHAP|).

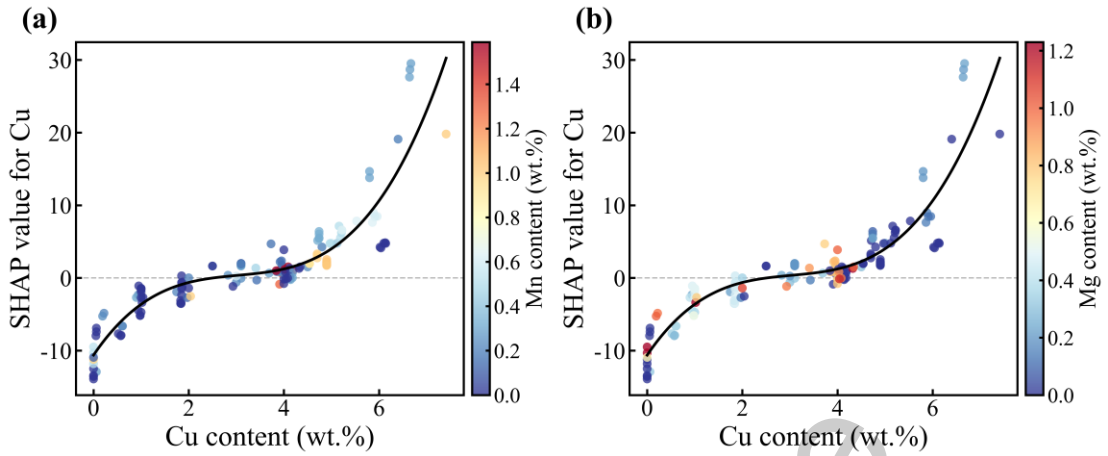

Figure 10. SHAP dependence plots for Cu content. (a) Colored by Mn content; (b) Colored by Mg content. The black fitted curve represents the overall trend between the Cu content and its SHAP value, while the color of the scatter points reflects the relative concentration of the corresponding modulating elements.

CONCLUSION

This study constructed a machine learning (ML) model for predicting the ultimate tensile strength (UTS) of heat-resistant cast aluminum alloys, and synergistically designed the alloy composition and heat treatment parameters by incorporating a genetic algorithm (GA). The reliability of the model's predictions was experimentally validated. An enhancement in UTS at 300 °C was achieved, and the underlying strengthening mechanisms were elucidated, demonstrating that this data-driven approach exhibits significant advantages over traditional trial-and-error experimental methods. The main conclusions are as follows:

(1) Through a three-stage feature selection strategy-comprising Pearson correlation screening, Random Forest (RF) importance ranking, and exhaustive search-an ML predictive model with robust forecasting capability was constructed for high-strength, heat-resistant cast aluminum alloys. The coefficient of determination (R^2) of this model for UTS reached 0.88.

(2) A novel alloy exhibiting excellent high-temperature strength, designated as ZL-2 (Al-5.96Cu-2.9Mg-0.42Ti-1.35Mn), was rapidly designed based on the genetic algorithm. At 300 °C, the UTS of the ZL-2 alloy reached 214.2 MPa, representing an increase of 61.0% and 25.1% compared to the reference alloys ZL114A (133.0 MPa)

and ZL205A (171.2 MPa), respectively.

(3) The superior elevated-temperature strength of ZL-2 is mainly attributed to the synergistic strengthening of multiscale secondary phases. The coexistence of nanoscale Mn-rich $Al_{20}Cu_2Mn_3$ precipitates, finer Al_2CuMg precipitates, and micron-scale Al_3Ti-containing intermetallics provides an important microstructural basis for the strength retention of ZL-2 at 300 °C.

(4) The modeling and optimization approach proposed in this study can serve as a valuable reference for the research and development of heat-resistant aluminum alloys and other high-temperature structural materials.

In future work, DFT-derived descriptors, including phase formation energy, solute binding energy, lattice misfit, interfacial energy, and diffusion barriers, could be incorporated into the present machine-learning framework to establish a hybrid DFT-ML strategy, thereby further improving the physical interpretability and transferability of heat-resistant aluminum alloy design.

DECLARATIONS

Authors' contributions

Changmei Hao: Writing - review & editing, Writing - original draft, Visualization, Validation, Methodology, Investigation, Formal analysis, Data curation, Conceptualization.

Peng Kuai: Writing - review & editing, Validation, Investigation.

Jianhua Duan: Writing - review & editing, Validation, Methodology, Formal analysis.

Shaolei Yang: Writing - review & editing, Formal analysis.

Yudong Sui: Writing - review & editing, Validation, Supervision, Investigation, Funding acquisition.

Yehua Jiang: Writing - review & editing, Validation, Supervision, Project administration, Methodology, Investigation, Conceptualization.

Han Xiao: Writing - review & editing, Validation, Supervision, Investigation

Availability of data and materials

Some results supporting the study are presented in the Supplementary Materials. Other

raw data that support the findings of this study are available from the corresponding author upon reasonable request.

AI and AI-assisted tools statement

Not applicable.

Financial support and sponsorship

This work was supported by the National Natural Science Foundation of China [grant number 52575391], Science and Technology Major Project of Yunnan Province [grant number 202502AB080012], and project funds of "Xingdian Talent Support Program".

Conflicts of interest

All authors declared that there are no conflicts of interest.

Ethical approval and consent to participate

Not applicable.

Consent for publication

Not applicable.

REFERENCES

1. Javidani, M. & Larouche, D. Application of cast Al-Si alloys in internal combustion engine components. Int Mater Rev. 59, 132-158(2014). DOI: 10.1179/1743280413Y.0000000027

2. Timelli, G., Caliari, D., & Rakhmonov, J. Influence of process parameters and Sr addition on the microstructure and casting defects of LPDC A356 alloy for engine blocks. J Mater Sci Technol. 32(6), 515-523(2016). DOI: 10.1016/j.jmst.2016.03.010

3. Yan, J., Tong, Q., Zhang, W., Yuan, Y., Jin, S., Guo, Z., ... & Cao, Z. Research on accelerated thermal fatigue testing and life prediction of Al-Si alloy pistons under start-stop cycles. Int J Fatigue. 191, 108677(2025). DOI: 10.1016/j.ijfatigue.2024.108677

4. Xiong, P., Liu, S., Li, Z., Deng, L., Guo, J., Shi, L., ... & Qiao, X. A new accelerated

thermal fatigue experiment method of pistons and its application. Eng Fail Anal. 163, 108599(2024). DOI: 10.1016/j.engfailanal.2024.108599

5. Roy, S., Allard, L. F., Rodriguez, A., Watkins, T. R., & Shyam, A. Comparative evaluation of cast aluminum alloys for automotive cylinder heads: part I—microstructure evolution. Metall Mater Trans A. 48, 2529-2542(2017). DOI: 10.1007/s11661-017-3985-1

6. Rakhmonov, J., Liu, K., Pan, L., Breton, F., & Chen, X. G. Enhanced mechanical properties of high-temperature-resistant Al-Cu cast alloy by microalloying with Mg. J Alloy Compd. 827, 154305(2020). DOI: 10.1016/j.jallcom.2020.154305

7. Jiang, L., Rouxel, B., Langan, T., & Dorin, T. Coupled segregation mechanisms of Sc, Zr and Mn at θ′ interfaces enhances the strength and thermal stability of Al-Cu alloys. Acta Materialia, 206, 116634(2021). DOI: 10.1016/j.actamat.2021.116634

8. Bansal, U., Singh, M. P., Mondol, S., Sinha, S. K., Makineni, S. K., Paul, A., & Chattopadhyay, K. The interplay of precipitation of ordered compounds and interfacial segregation in Al-Cu-Hf-Si alloys for high-temperature strength. Acta Materialia, 240, 118355(2022). DOI: 10.1016/j.actamat.2022.118355

9. Wu, Y., Chen, Z., Le, W., Zhang, H., Song, W., & Yang, Z. Optimization of high-temperature mechanical properties of aluminum alloys through exclusive precipitation of T-phase. J Mater Res Technol. 33, 3144-3154(2024). DOI: 10.1016/j.jmrt.2024.09.261

10. Booth-Morrison, C., Dunand, D. C., & Seidman, D. N. Coarsening resistance at 400 C of precipitation-strengthened Al-Zr-Sc-Er alloys. Acta Mater. 59, 7029-7042 (2011). DOI: 10.1016/j.actamat.2011.07.057

11. Gao, Y. H., Yang, C., Zhang, J. Y., Cao, L. F., Liu, G., Sun, J., & Ma, E. Stabilizing nanoprecipitates in Al-Cu alloys for creep resistance at 300 C. Mater Res Lett. 7, 18-25(2019). DOI: 10.1080/21663831.2018.1546773.

12. Yang, J., Ni, Y., Li, H., Fang, X., & Lu, B. Heat treatment optimization of 2219 aluminum alloy fabricated by wire-arc additive manufacturing. Coatings, 13, 610(2023). DOI: 10.3390/coatings13030610

13. Gariboldi, E., & Sharma, A. Enhancing Thermal Stability and High-Temperature Properties of Foundry Al Alloys through Zr and/or Er as Minor Alloying Elements. Int J Metalcast. 3552-3565(2025). DOI: 10.1007/s40962-025-01549-z

14. Qi, Y., Zhang, H., Yang, X., Wang, Y., Han, C., Fan, W., ... & Zhu, H. Achieving superior high-temperature mechanical properties in Al-Cu-Li-Sc-Zr alloy with nano-

scale microstructure via laser additive manufacturing. Mater Res Lett. 12, 17-25(2024). DOI: 10.1080/21663831.2023.2285388

15. Lu, Q., Wang, J., Li, H., Jin, S., Sha, G., Lu, J., ... & Du, Y. Synergy of multiple precipitate/matrix interface structures for a heat resistant high-strength Al alloy. Nat Commun. 14, 2959(2023). DOI: 10.1038/s41467-023-38730-z

16. Mondol, S., Makineni, S. K., Kumar, S., & Chattopadhyay, K. Enhancement of high temperature strength of 2219 alloys through small additions of Nb and Zr and a novel heat treatment. Metall Mater Trans A. 49, 3047-3057(2018). DOI: 10.1007/s11661-018-4614-3

17. Mondol, S., Kashyap, S., Kumar, S., & Chattopadhyay, K. Improvement of high temperature strength of 2219 alloy by Sc and Zr addition through a novel three-stage heat treatment route. Mat Sci Eng A-Struct. 732, 157-166 (2018). DOI: 10.1016/j.msea.2018.07.003

18. Cheng, S., Yi, W., Zhang, M., Gao, T., & Zhang, L. Forward versus inverse design of Al-Si-Mg-Cu alloys targeting peak comprehensive mechanical properties: a comparative study integrating computational thermodynamics and active learning. Acta Mater. DOI: 10.1016/j.actamat.2026.121930

19. Jiang, L., Zhang, Z., Hu, H., He, X., Fu, H., & Xie, J. A rapid and effective method for alloy materials design via sample data transfer machine learning. Npj Comput Mater. 9, 26 (2023). DOI: 10.1038/s41524-023-00979-9

20. Yin, J., Lei, Q., Li, X., Zhang, X., Meng, X., Jiang, Y., ... & Li, Z. A novel neural network-based alloy design strategy: Gated recurrent unit machine learning modeling integrated with orthogonal experiment design and data augmentation. Acta Mater. 243, 118420 (2023). DOI: 10.1016/j.actamat.2022.118420

21. Yang, C., Ren, C., Jia, Y., Wang, G., Li, M., & Lu, W A. machine learning-based alloy design system to facilitate the rational design of high entropy alloys with enhanced hardness. Acta Mater. 222, 117431 (2022). DOI: 10.1016/j.actamat.2021.117431

22. Wang, J., Kwon, H., Oh, S. H., Lee, J. H., Yun, D. W., Lee, H., ... & Lee, B. J. Multiscale computational framework linking alloy composition to microstructure evolution via machine learning and nanoscale analysis. Npj Comput Mater. 11, 230 (2025). DOI: 10.1038/s41524-025-01730-2

23. Kavousi, S., & Zaeem, M. A. Integration of multiscale simulations and machine learning for predicting dendritic microstructures in solidification of alloys. Acta Mater. 289, 120860 (2025). DOI: 10.1016/j.actamat.2025.120860

24. Jiang, L., Fu, H., Zhang, Z., Zhang, H., Zhang, X., Feng, X., ... & Xie, J. Synchronously enhancing the strength, toughness, and stress corrosion resistance of high-end aluminum alloys via interpretable machine learning. Acta Mater. 270, 119873 (2024). DOI: 10.1016/j.actamat.2024.119873

25. Jiang, L., Zhoutai, W., Zhang, X., Shi, Z., Han, Z., Cui, Y., & Xie, J. Interpretable machine learning design for concurrent and significant enhancement of the mechanical properties and corrosion resistance of low-density Mg-Li alloys. J. Magnes. Alloy. (2025). DOI: 10.1016/j.jma.2025.10.014

26. Hu, M., Tan, Q., Knibbe, R., Xu, M., Liang, G., Zhou, J., ... & Zhang, M. X. Designing unique and high-performance Al alloys via machine learning: Mitigating data bias through active learning. Comp Mater Sci. 244, 113204 (2024). DOI: 10.1016/j.commatsci.2024.113204

27. Li, Y., Pang, J., Li, Z., Wang, Q., Wang, Z., Li, J., ... & Liaw, P. K. Developing novel low-density high-entropy superalloys with high strength and superior creep resistance guided by automated machine learning. Acta Mater. 285, 120656 (2025). DOI: 10.1016/j.actamat.2024.120656

28. He, S., Xiao, F., Li, L., Liu, Y., Zeng, Y., Gong, M., ... & Jin, X. Design biomedical β-Ti alloys with exceptional strength-ductility balance via domain knowledge-based machine learning. Acta Mater. 121550 (2025). DOI: 10.1016/j.actamat.2025.121550

29. Guru, M. K., Bohlen, J., Aydin, R. C., & Khalifa, N. B. Machine learning pipeline for Structure-Property modeling in Mg-alloys using microstructure and texture descriptors. Acta Mater. 121132 (2025). DOI: 10.1016/j.actamat.2025.121132

30. Pedregosa, F., Varoquaux, G., Gramfort, A., Michel, V., Thirion, B., Grisel, O., ... & Duchesnay, É. Scikit-learn: Machine learning in Python. J Mach Learn Res. 12, 2825-2830 (2011). https://dl.acm.org/doi/10.5555/1953048.2078195

31. Lundberg, S. M., & Lee, S. I. A unified approach to interpreting model predictions. Adv Neural Inf Process Syst, 30 (2017). https://dl.acm.org/doi/10.5555/3295222.3295230

32. Jiang, L. T. Effect of heat treatment on microstructure and dimensional stability of ZL114A aluminum alloy. T Nonferr Metal Soc. 20, 2124-2128 (2010). DOI: 10.1016/S1003-6326(09)60428-3

33. Li, Y., Zhang, G. W., & Xu, H. Study on heat treatment process for ZL205A alloy. Foundry Technol, 38, 68 (2017). DOI: 10.16410/j.issn1000-9365.2017.01.018

34. Xu, S., Khanlari, K., Lin, B., Fan, T., Xia, S., Achouri, I. E., ... & Jiang, Y. Effects

of Fe-addition as a beneficial modifying element on the microstructure and mechanical properties of an Al-Si-Cu-Mg-Ni-Mn piston alloy. Metallogr Microstruct Anal. 12, 401-412 (2023). DOI: 10.1007/s13632-023-00939-1

35. Liao, H. C., Xu, H. T., & Hu, Y. Y. Effect of RE addition on solidification process and high-temperature strength of Al- 12% Si-4% Cu- 1.6% Mn heat-resistant alloy. Trans. Nonferrous Met. Soc. China, 29(6), 1117-1126 (2019). DOI: 10.1016/S1003-6326(19)65020-X

36. Chen, J., Liao, H., Wu, Y., & Li, H. Contributions to high temperature strengthening from three types of heat-resistant phases formed during solidification, solution treatment and ageing treatment of Al-Cu-Mn-Ni alloys respectively. Mat Sci Eng A-Struct, 772, 138819 (2020). DOI: 10.1016/j.msea.2019.138819

37. Li, G., Liao, H., Zheng, J., Yang, M., Qian, L., Shi, M., & Lu, L. Synergistic effect of joint addition of Sb+ Mn on high temperature strengthening in Al-4Cu heat-resistant alloy. Mat Sci Eng A-Struct, 851, 143623 (2022). DOI: 10.1016/j.msea.2022.143623

38. Li, G., Liao, H., Zheng, J., Chen, H., Lu, L., Yang, L., & Guo, H. Micro-alloying effects of Mn and Zr on the evolution of ageing precipitates and high temperature strength of Al-11.5 Si-4Cu alloy after a long-time heat exposure. Mat Sci Eng A-Struct, 828, 142121 (2021). DOI: 10.1016/j.msea.2021.142121

39. Chen, J., Liao, H., & Xu, H. Uneven Precipitation Behavior during the Solutionizing Course of Al-Cu-Mn Alloys and Their Contribution to High Temperature Strength. Adv Mater Sci Eng, 2018(1), 6741502 (2018). DOI: 10.1155/2018/6741502

40. Su, R., Xiao, J., Jia, Y., Wang, K., & Qu, Y. Study on properties and microstructure of an Al-Cu-Mg-Fe-Ni alloy with two-stage aging treatment. Mater Res Express, 6(12), 126561 (2019). DOI: 10.1088/2053-1591/ab5909

41. Lin, B., Zhang, W., Zheng, X., Zhao, Y., Lou, Z., & Zhang, W. Developing high performance mechanical properties at elevated temperature in squeeze cast Al-Cu-Mn-Fe-Ni alloys. Mater Charact, 150, 128-137 (2019). DOI: 10.1016/j.matchar.2019.01.022

42. Ritchie, R. The conflicts between strength and toughness. Nature Mater. 10, 817-822 (2011). DOI: 10.1038/nmat3115

43. Ma, Y., Chen, H., Zhang, M. X., Addad, A., Kong, Y., Lezaack, M. B., ... & Ji, G. Break through the strength-ductility trade-off dilemma in aluminum matrix composites via precipitation-assisted interface tailoring. Acta Mater. 242, 118470 (2023). DOI: 10.1016/j.actamat.2022.118470

44. Ma, Y., Wang, Q., Jiang, B. B., Li, C. L., Hao, J. M., Li, X. N., ... & Nieh, T. G. Controlled formation of coherent cuboidal nanoprecipitates in body-centered cubic high-entropy alloys based on Al2 (Ni, Co, Fe, Cr) 14 compositions. Acta Mater. 147, 213-225 (2018). DOI: 10.1016/j.actamat.2018.01.050

45. Ma, Y., Hao, J., Jie, J., Wang, Q., & Dong, C. Coherent precipitation and strengthening in a dual-phase AlNi2Co2Fe1. 5Cr1. 5 high-entropy alloy. Mat Sci Eng A-Struct. 764, 138241 (2019). DOI: 10.1016/j.msea.2019.138241

46. Klenam, D., Bamisaye, O., Asumadu, T., Bodunrin, M., & Soboyejo, W. Solving the strength-ductility trade-off using complex concentrated alloy design strategy: An overview. SMMF. 3, 100091 (2025). DOI: 10.1016/j.smmf.2025.100091

47. Seidman, D. N., Marquis, E. A., & Dunand, D. C. Precipitation strengthening at ambient and elevated temperatures of heat-treatable Al (Sc) alloys. Acta Mater, 50(16), 4021-4035 (2002). DOI: 10.1016/S1359-6454(02)00201-X

48. Koju, R. K., & Mishin, Y. Atomistic study of grain-boundary segregation and grain-boundary diffusion in Al-Mg alloys. Acta Mater, 201, 596-603 (2020). DOI: 10.1016/j.actamat.2020.10.029

49. Belov, N. A., Alabin, A. N., & Matveeva, I. A. Optimization of phase composition of Al-Cu-Mn-Zr-Sc alloys for rolled products without requirement for solution treatment and quenching. J Alloy Compd, 583, 206-213 (2014). DOI: 10.1016/j.jallcom.2013.08.202

50. Liao, H., Tang, Y., Suo, X., Li, G., Hu, Y., Dixit, U. S., & Petrov, P. Dispersoid particles precipitated during the solutionizing course of Al-12 wt% Si-4 wt% Cu-1.2 wt% Mn alloy and their influence on high temperature strength. Mat Sci Eng A-Struct, 699, 201-209 (2017). DOI: 10.1016/j.msea.2017.04.091

51. Wolverton, C. J. A. M. Crystal structure and stability of complex precipitate phases in Al-Cu-Mg-(Si) and Al-Zn-Mg alloys. Acta Mater, 49(16), 3129-3142 (2001). DOI: 10.1016/S1359-6454(01)00229-4

52. Gazizov, M. R., Belyakov, A. N., Holmestad, R., Gazizova, M. Y., Krasnikov, V. S., Bezborodova, P. A., & Kaibyshev, R. O. The coarsening behavior of strengthening particles in an Al-Cu-Mg-Ag alloy during creep. Mat Sci Eng A-Struct, 884, 145515 (2023). DOI: 10.1016/j.msea.2023.145515

53. Chen, X. J., Wang, B., Wang, Z., Zhang, D. Y., Wang, H., Li, J. H., ... & Wang, S. B. Unveiling micromechanism of Fe minor addition-induced property degradation of an Al-5.1 Cu-0.65 Mg-0.8 Mn (wt%) alloy. Rare Metals, 44(5), 3496-3513 (2025). DOI:

10.1007/s12598-024-03175-w

54. Lu, G., Sun, B., Wang, J., Liu, Y., & Liu, C. High-temperature age-hardening behavior of Al-Mg-Si alloys with varying Sn contents. J Mater Res Technol, 14, 2165-2173 (2021). DOI: 10.1016/j.jmrt.2021.07.122

55. Hu, K., Zou, C., Wang, H., & Wei, Z. The role of in-situ Al3Ti formed during solidification in improving the high-temperature properties of Al-Cu alloy. Mat Sci Eng A-Struct, 902, 146585 (2024). DOI: 10.1016/j.msea.2024.146585

56. Bate, P. The effect of deformation on grain growth in Zener pinned systems. Acta Mater, 49(8), 1453-1461 (2001). DOI: 10.1016/S1359-6454(01)00033-7